Retrieval of daytime mesospheric ozone using OSIRIS observation of $O_2(a^1\Delta_g)$ emission

Anqi Li[1], Chris Roth[2], Kristell Pérot[1], Ole Martin Christensen[1], Adam Bourassa[2], Doug Degenstein[2], and Donal Murtagh[1]

[1]Chalmers university of technology, Department of Space, Earth and Environment, Gothenburg, Sweden
[2]Institute of Space and Atmospheric Studies, University of Saskatchewan, Saskatoon, Canada

Correspondence: Anqi Li (anqi.li@chalmers.se)

Abstract. Improving knowledge of the ozone global distributions in the mesosphere-lower thermosphere (MLT) is a crucial step in understanding the behaviour of the middle atmosphere. However, the ozone concentration under sunlit conditions in the MLT is often so low that its measurement requires instruments with very high sensitivity. Fortunately, the bright oxygen airglow can serve as a proxy to retrieve the daytime ozone density indirectly, due to the strong connection to ozone photolysis in the

5   Hartley band. The OSIRIS IR imager (hereafter IRI), one of the instruments on the Odin satellite, routinely measures the oxygen infrared atmospheric band (IRA band) at $1.27\,\mu m$. In this paper, we will primarily focus on the description of the detailed steps for retrieving the calibrated IRA band limb radiance, the volume emission rate of $O_2(a^1\Delta_g)$ and, finally, the ozone number density. This retrieval technique is applied to a one-year-sample IRI dataset. The resulting product is a completely new ozone dataset with very high along-track resolution. The performance of the retrieval technique is demonstrated by a comparison

10   of the coincident ozone measurements from the same spacecraft, as well as zonal mean and monthly average comparisons between OS, SMR, MIPAS and ACE-FTS. The consistency of this IRI ozone dataset implies that such a retrieval technique can be further applied to all the measurements made throughout the 19 years-long mission, leading to a long-term, high resolution dataset in the middle atmosphere.

15 # 1   Introduction

The distribution of ozone plays a key role in the middle atmosphere, such that it can influence the radiative budget, affecting temperature structures and the dynamic flow patterns (Brasseur and Solomon, 2005). As such, attention has been drawn to the observations of ozone over the past decades. The existence of the stratospheric ozone layer, resulting from the absorption in the Herzberg continuum, was proposed early last century and subsequently confirmed (Chapman, 1930). Near the mesopause

20 region, a secondary ozone layer, which is the result of radiation absorption in the Schumann-Runge continuum, was detected (Hays and Roble, 1973). More recently, the existence of a tertiary ozone maximum was discovered by multiple measurements

both from ground-based and satellite instruments (e.g., Marsh et al., 2001). The tertiary ozone maximum only occurs in winter, in the high-latitude middle mesosphere. The mechanism behind it is mainly due to a decrease in atomic oxygen losses involving the odd-hydrogen species near the polar night terminator. However, the detailed picture of the tertiary ozone maximum is not

25   yet fully explained because of the complexities in both the chemical composition and the dynamics of the mesosphere and lower thermosphere (MLT) (e.g., Hartogh et al., 2004; Degenstein et al., 2005a; Sofieva et al., 2014; Smith et al., 2018).

Satellite observations provide us with valuable knowledge on the behaviour of atmospheric ozone. In the MLT region, various measurement techniques are employed to monitor the ozone distribution. For instance, there are observations of ozone absorption by using solar or stellar occultation (e.g. HALOE, ACE-FTS, SOFIE, GOMOS) (all acronyms are given in Table

30   A2), of emission from thermally excited ozone (e.g. SABER at $9.6\,\mu m$, MIPAS, SMR) and of airglow emission (SME, SABER and SCIAMACHY at $1.27\,\mu m$, OSIRIS at $762\,nm$). Smith et al. (2013) have shown comparisons of ozone concentrations in the MLT region resulting from most of the above mentioned techniques. They have concluded from coincident profile comparisons that different measurement principles agree with each other reasonably well (better than 20% for the instruments considered here). However, they emphasise that the differences in local time sampling among the measurements affect the inferred global

35   distribution in the MLT, for instance, the vertical structure and seasonal variations of ozone. Other than differences in measurement principle and sampling schedules, uncertainties in the calibration and band-passes of the instrument and inaccurate pointing knowledge may also contribute to the difference between these ozone observations. Furthermore, the photochemical timescales of the airglow species critically affect the inferred ozone distribution, especially whose lifetime is comparable to the transport timescales. The $1.27\,\mu m$ emission has a photochemical lifetime of about 74 minutes which can affect the measure-

40   ments in two ways. One is the effect of transport and the other can be the delay in reaching quasi-photochemical equilibrium after sunrise. Zhu et al. (2007) have evaluated the uncertainties in daytime ozone retrieved from $1.27\,\mu m$ emission due to the effect of tidal waves and the photochemical steady state assumption, by using a dynamical-photochemical coupled airglow model.

In this study, we will focus on the retrieval of the ozone data collected by instruments aboard the Odin satellite, particularly

45   the OSIRIS IR imager (hereafter IRI). The Odin satellite is orbiting the Earth around 15 times per day since 2001 and is still fully functional (Murtagh et al., 2002). SMR (Submillimeterwave Radiometer) and OSIRIS (Optical Spectrograph and Infrared Imaging System) are the two main components on Odin. Both of them measure various species closely related to the ozone chemistry by observing the Earth's limb. Furthermore, OSIRIS includes two optically independent instruments: the optical spectrograph (hereafter OS) and the infrared imager. IRI has three vertical imagers. Two of them measure the oxygen infrared

50   atmospheric band (IRA band) emissions centred at $1.27\,\mu m$, and the third one measures the OH Meinel band emission centred at $1.53\,\mu m$. A more detailed description of IRI can be found in Sect. 2.1 as well as in Llewellyn et al. (2004). Data collected by one of the oxygen IRA band imagers have been studied by Degenstein et al. (2004) to demonstrate a tomographic retrieval technique to derive airglow volume emission rate and its comparison to non-tomographic retrieved volume emission rate. Degenstein et al. (2005b) showed the potential of the IRI observations for estimating ozone depletion during a Solar Proton

55   Event. The observations of oxygen IRA band and the OH Meinel band together were used to study the mesospheric tertiary

ozone peak by Degenstein et al. (2005a). To our knowledge, there is no further investigation which deals with the dataset from the IRI instrument.

Our primary objective in this paper is to revisit the oxygen airglow measurements obtained from the IRI at 1.27 µm and demonstrate a retrieval scheme used to derive the volume emission rate as well as the ozone concentration in the MLT region

60 based on Bayesian estimation. This ozone product will be a completely new dataset from the Odin mission and is complementary to the already existing ozone measurements since the signal strength in the MLT region during daytime is often too low for the other instruments. In addition, this IRI ozone product has about 70 times higher along-track sampling rate than the other ozone products thanks to the imaging technique.

To illustrate the performance of the retrieval technique, a small but representative sample of the IRI measurements collected

65 from November 2007 to October 2008 have been processed. Our secondary focus is to demonstrate the fidelity of the resulting new IRI ozone product by a side-by-side comparison with other independent ozone measurements, namely OS, SMR, MIPAS and ACE-FTS ozone products. However, we would like to emphasise that this paper is not intended to be a full validation study. IRI, OS and SMR observe at the same geographical location and time because they are on board the same platform, thus the bias due to the different sampling schedules mentioned in Smith et al. (2013) is negligible. However, due to their differences in

70 altitude coverage, we also include MIPAS and ACE-FTS ozone profiles, measurements retrieved from other satellites, in our comparison to give a more complete picture of the global nature of the agreement. Their demonstrated consistency indicates that the presented IRI ozone retrieval scheme can be applied to the whole 19 years of the mission to date, opening new opportunities to perform further scientific studies.

Also, we want to highlight that it is novel to illustrate how the three ozone data sets from Odin complement each other so

75 well, despite their intrinsically different underlying physical bases in terms of measurement techniques. For a broader scientific community, we demonstrate that Odin can cover a large part of the atmosphere using its different instruments.

2 Theory and implementation

In this section, we will discuss the necessary steps to derive the calibrated limb radiance (in Sect. 2.1), then the volume emission rate of the oxygen IRA band (in Sect. 2.2) and, finally, the ozone number density profiles (in Sect. 2.3). The theoretical

80 background, as well as the implementation details can be found in the corresponding subsections.

2.1 Level 1 data – calibrated limb radiance data

The IRI instrument measures the oxygen IRA band with 10 µm wide filters centered at 1.273 µm and 1.263 µm (channels 2 and 3, respectively, in OSIRIS nomenclature) and the OH Meinel emissions with 40 µm wide filter centered at 1.530 µm (channel 1) (Degenstein et al., 2004). All three of the single-lens IR imagers consist of a linear array of 128 InGaAs photodiodes

85 (pixels). Each array is split into two sections: a masked off, permanently dark portion of approximately twenty pixels used for calibration, and the remaining pixels used for data collection. The optical portion of the IRI instrument was designed such that the angular spacing between photodiodes results in approximately 1 km separation between the tangent altitudes of the look

vectors. Each image of the IRI system consists of a measurement of each of the 128 pixels. Images are taken approximately
every two seconds with a one-second duration exposure time.

90   Like any photodetection system, the IRI must be calibrated to remove instrument dependent effects from the measurement
and convert the digital count into calibrated radiance. This calibration process occurs in four steps: (1) dark current and elec-
tronic offset, (2) relative calibration of the pixel gain, (3) removal of stray light, and (4) absolute calibration. The calibration
process applied to the IRI data used in this work is an updated version of (Bourassa, 2003). A short description of each step
follows.

95   In this paper, we will only look at data taken from channel 3 centred at $1.263\,\mu\text{m}$.

2.1.1 Dark Current and Electronic Offset

Each of the 128 pixels in the linear array of photodiodes has a unique temperature dependent dark current characteristic. The
signal is referred to as "dark current" as it is thermally generated and present regardless of whether or not the photodiode is
subject to light (photons). As is typical of semiconductor systems this small number of thermally generated electron-hole pairs
100   have a Poisson distribution and follow the Shockley equation.

The electron-hole diffusion current and recombination current are proportional to

$$e^{-E_g/k_B T} \tag{1}$$

and

$$e^{-E_g/2k_B T}, \tag{2}$$

105   respectively, where E_g is the band gap energy, T, the temperature, and k_B, Boltzmann's constant.

In practice, each pixel's unwanted thermal signal can be characterised by a single exponential term of the form

$$\gamma_i e^{\beta_i/T}, \tag{3}$$

for each pixel i in the array, where γ and β are parameters found by implementing least-squares curve fitting to the data.

In addition to the removal of the dark current, two sources of electronic offset must also be characterised and removed from
110   the measurements. The first is a relatively time-invariant electronic offset that is unique to each pixel. By adding a parameter
that characterises each pixel's unique electronic offset to the above equation, a three-parameter fit is used for each pixel

$$\alpha_i + \gamma_i e^{\beta_i/T} \tag{4}$$

where α is the offset parameter. The second form of electronic offset is the same for each pixel, but varies randomly with each
image due to noise in the electronics. This is handled separately from the three-parameter fit.

115   Calibration data for the IRI instrument, where an optical shutter is closed to block out incoming light, is used to compute the
three parameters (for each pixel) at regular intervals throughout the mission. The fitting process is a periodized, least-squares
optimisation.

Atmospheric
Measurement
Techniques
Discussions

By applying the parameters found using the calibration data to the data collection portion of the mission where the optical shutter is open, the dark current and the pixel dependent electronic offset are removed from the raw data. The image dependent

120   electronic offset can then be determined, and subtracted off, using the permanently dark masked off pixels.

In short, this step calibrates each photodiode's measurement to zero (within measurement error consistent with shot noise) when not exposed to light.

2.1.2   Relative Calibration of the Pixels

In this step, referred to as the relative calibration or pixel "flat fielding", each pixel's output is normalised so that a uniform

125   input brightness on each pixel results in the same digital counts. Prior to launch, the instrument was subjected to a calibrated Lambertian light source to determine these parameters, but early mission data revealed that the pre-launch relative calibration curves were no longer accurate.

To perform an in-flight relative calibration of the pixels, the mesospheric night-time airglow layer was used in place of a calibrated Lambertian source. As the IRI instrument scans up and down through this layer, comparisons are made between

130   neighbouring pixels as they pass through the same layer to derive this relative gain factor for each pixel. Although the airglow layer is not constant in brightness, the statistical impact of this variation becomes negligible as the number of intercomparisons becomes large. The relative calibration algorithm was applied to every applicable night time orbit. The resulting data was averaged to create an in-flight relative calibration curve that is applied to the IRI data. The in-flight curves closely resemble the pre-flight curves with notable differences towards the edges of the arrays.

135   2.1.3   Stray Light Removal

It is evident from the IRI data that off-axis light from the sunlit Earth is incident on the IR detectors due to scattering and diffraction. An in-depth modelling of the IRI optical system was performed by Ivanov (2000). This work and Bourassa (2003) finds that during the sunlit portions of the orbit, the measured signal is the sum of the atmospheric brightness and a large unwanted stray light signal from the off-axis Earth below.

140   To remove the stray light, its shape is first characterised using data where the amount of real incident light is negligible. This occurs when the pixel look direction tangent points are over $100\,\mathrm{km}$. The shape of the stray light is then extrapolated to lower tangent altitudes and the magnitude of stray light for any image is assumed to be proportional to the average brightness of the pixels over $100\,\mathrm{km}$. As the number of pixels over $100\,\mathrm{km}$ changes from image to image due to the nodding nature of the Odin spacecraft, the quality of the stray light removal process changes; becoming less accurate when fewer pixels are present over

145    $100\,\mathrm{km}$. This decrease in accuracy is accounted for in the error estimate of the data related to the stray light removal process.

2.1.4   Absolute Calibration

Finally, the data is multiplied by a factor to convert the digital number measurement of the read-out electronics to a measurement of calibrated radiance reported in $\frac{\mathrm{photons}}{\mathrm{s \cdot cm^2 \cdot sterad}}$, or photons per second from a unit area within a unit solid angle. The usual

per nm wavelength dependence of the radiance, common in remote sensing observations of a spectrum, it is not used in this formulation as the measurement is an integral over the infrared band filter.

The absolute calibration value used to convert the data from digital counts to brightness was determined through calibration sessions pre-launch. Post-launch the calibration value for the $1.53\,\mu m$ channel was checked by comparing it to a standard single Rayleigh scattering model of the atmosphere, which showed that the pre-launch value was still applicable. As there is no equivalent simple atmospheric model to test against the $1.27\,\mu m$, and there has been no evidence to conclude otherwise, the assumption is that the absolute calibration values for channels 2 and 3 are also still applicable.

2.1.5 Calibration Error

Throughout each step in the calibration process, uncertainties are calculated so that the uncertainty values given with the final calibrated data are meaningful and accurate.

To begin with, the error in the measured digital number of read-out electronics is a combination of two sources: the shot noise of the detector and the random error due to the fact that the number of photons incident on the pixel array follows a Poisson distribution (which is negligibly small for all but the brightest of scenes.)

The final reported error also incorporates the error in the pixel electronics offset, and is the combination of the errors determined through the various calibration steps: the error in pixel electronics offset and thermal characteristics, the error in the relative calibration curve, and finally the error in the stray light calibration table.

Figure 1 shows the radiance profile of a sample IRI exposure. The vertical axis is tangent height of the pixel's look direction rather than pixel number. For daytime exposures, a total error between 1-10% is typical with the stray light error as the largest contributing factor.

2.2 Retrieval of $O_2(a^1\Delta_g)$ airglow volume emission rate

Once we have obtained the calibrated limb radiance, the next quantity to derive is the volume emission rate, since the volume emission rate of photons emitted in the oxygen infrared atmospheric band is directly related to the number density of $O_2(a^1\Delta_g)$ by its radiative lifetime (i.e. Einstein A coefficient). In this paper, only daytime measurements are considered since we rely on a photochemical scheme, described in Sect. 2.3, to derive the ozone number density. However, IRI also collects high quality data in the night part of the orbits (not shown) which will be valuable for other studies.

We will use a linearized scheme to retrieve volume emission rate profiles. The retrieval problem becomes linear if we assume that the majority of the signal originates from the tangent layer emissions. However, this means that data measured at tangent altitudes lower than a certain level should not be included for the analysis as the measured signal becomes dominated by properties of other atmospheric layers due to absorption and scattering processes. Degenstein (1999) has indicated that self-absorption of the oxygen IRA band becomes significant when line-of-sight tangent is lower than $60\,km$. Hence we use this as a lower bound of limb radiance data selection. An upper bound of 100 km line-of-sight tangent height is chosen due to the weak emission signal above the airglow layer.
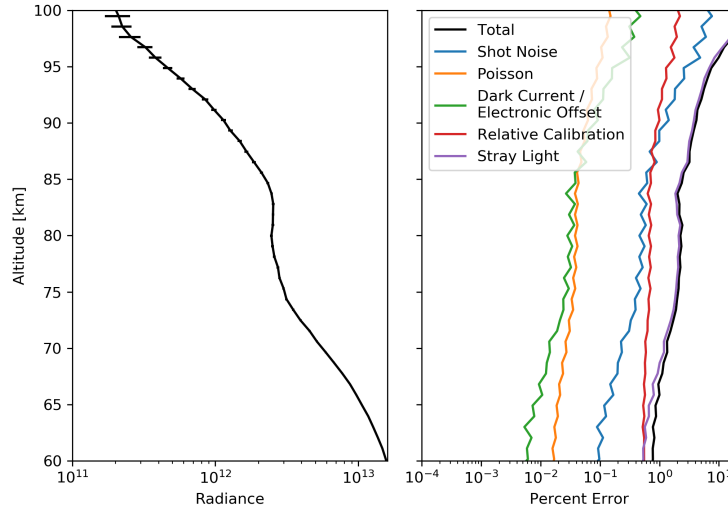
Figure 1. Left: A sample daytime exposure of IRIS radiance data (image 1250 of orbit 37400). Right: The corresponding total error and error contributions.

The IR imager measures the limb radiance R which is described by the radiative transfer equation

$$R = \frac{\phi}{4\pi} \int V(s) e^{-\tau(s)} \mathrm{d}s, \tag{5}$$

where $V(s)$ is the volume emission rate over the full band at location s along the line-of-sight of the instrument. ϕ is the 'filter factor' defined as the overlap between the instrument filter and the oxygen IRA band emission lines, and $e^{-\tau(s)}$ is the transmissivity between the emission source at s and the instrument along the line-of-sight. As previously explained, we assume no self-absorption, $e^{-\tau(s)}$ therefore simply becomes unity. ϕ is equal to 0.72 for the channel considered in this paper estimated from a simple spectral calculation using the HITRAN (Gordon et al., 2017) catalogue for the emission line strengths. The value of ϕ is relatively insensitive to the emission temperature. Thus the relationship between the measured limb radiance and volume emission rate becomes purely linear and can be expressed as

$$y_i = \sum_j k_{ij} x_j + \epsilon_i = \frac{4\pi R_i}{\phi}, \tag{6}$$

where y_i is the column emission rate for the full oxygen IRA band as would be measured by the pixel i (which is proportional to R_i), x_j the volume emission rate at the atmospheric layer j, k_{ij} the path length of the line-of-sight i through the atmospheric layer j and ϵ_i the measurement errors. In matrix notation, the relationship can thus be expressed as

$$\mathbf{y} = \mathbf{K}\mathbf{x} + \epsilon, \tag{7}$$

where $\mathbf{y}$ is also termed the measurement vector, $\mathbf{K}$ the weighting function, or Jacobian matrix and $\mathbf{x}$ the state vector.

Atmospheric
Measurement
Techniques
Discussions

Open Access
EGU

In this paper, the optimal estimation method (OEM), also known as the maximum a posteriori (MAP) method (Rodgers, 2000), is employed to invert the above equation. By constraining the inversion using the uncertainties of both the measured quantity and the a priori knowledge, the estimated profile of the volume emission rate can be expressed as

$$\hat{\mathbf{x}} = \mathbf{x_a} + \mathbf{G}(\mathbf{y} - \mathbf{K}\mathbf{x_a}), \tag{8}$$

200   where $\mathbf{x_a}$ denotes the a priori profile of volume emission rate, and $\mathbf{G}$ the gain matrix, which is equal to:

$$\mathbf{G} = (\mathbf{K^T}\mathbf{S_e^{-1}}\mathbf{K} + \mathbf{S_a^{-1}})^{-1}\mathbf{K^T}\mathbf{S_e^{-1}}, \tag{9}$$

where $\mathbf{S_e}$ and $\mathbf{S_a}$ are the error covariance matrices describing the uncertainties of the measurement $\mathbf{y}$ and of the a priori profile $\mathbf{x_a}$, respectively.

In our implementation, $\mathbf{x_a}$ is the $O_2(a^1\Delta_g)$ volume emission rate profile calculated by the photochemical model (see Sect.

205   2.3) by inputting the ozone profile from a climatology. This climatology was derived from the data presented by the Canadian Centre for Climate Modelling and Analysis known as the CMAM model [1] and evaluated for different latitudes, months and local solar times for the tangent points of the IRI measurements. The covariance matrix of the a priori follows

$$S_a(i,j) = \sigma_a(i)\,\sigma_a(j)\,\exp(|i - j|\frac{dz}{h}) \tag{10}$$

where $\sigma_\mathbf{a}$ is set to be $0.75\mathbf{x_a}$ and $dz/h = 1/5$. The off-diagonal elements act as a regularization on the estimation to prevent

210   oscillations. $\mathbf{S_e}$ has diagonal elements equal to the square of the uncertainty of each pixel (i.e. the calibration error described in Sect. 2.1). All off-diagonal elements for $\mathbf{S_e}$ are set to zero, that is assuming no correlation between errors for different pixels in the limb radiance measurements. The retrieval grid covers altitudes from $50\,\mathrm{km}$ to $130\,\mathrm{km}$ with $1\,\mathrm{km}$ spacing. Thus we have a $10\,\mathrm{km}$ and $30\,\mathrm{km}$ margin for the lower and upper bounds, respectively, in order to minimize any edge effect in the inversion process.

215   The vertical resolution of the retrieved data can be represented by the averaging kernel (AVK) matrix,

$$\mathbf{A} \equiv \frac{\partial\hat{\mathbf{x}}}{\partial\mathbf{x}} = \mathbf{G}\mathbf{K} \tag{11}$$

which maps the changes from the true state $\mathbf{x}$ to the estimated state $\hat{\mathbf{x}}$ at corresponding altitudes. The sum of each row of AVK matrix is termed the measurement response (MR) which describes how sensitive the estimated state is to true atmospheric state. However, it is more convenient, here, to assess AVK and MR relative to the a priori profile. This, because $\mathbf{x_a}$ exhibits a strong

220   vertical gradient and its covariance is scaled with $\mathbf{x_a}$ itself. As discussed in e.g. Baron et al. (2002); Hoffmann et al. (2011), the transformation from the ordinary AVK to the 'fractional AVK' matrix is given by,

$$A_{ij}^{frac} = x_a(j) \cdot A_{ij}/x_a(i). \tag{12}$$

Accordingly, the 'fractional MR' is given by,

$$MR_i^{frac} = \sum_j A_{ij}^{frac}. \tag{13}$$

---

[1] CMAM data is downloaded at http://climate-modelling.canada.ca/climatemodeldata/cmam/cmam30/
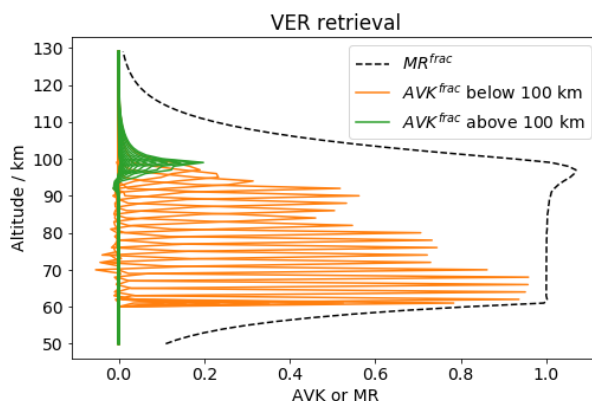
Figure 2. Every two rows of the fractional AVK (solid lines) and measurement response (black dashed line) from the retrieval of volume emission rate of the image 570 indicated in Fig. 3.

An example of the rows of the fractional AVK matrix and the corresponding MR of an inversion is shown in Fig. 2. As we can see these curves generally peak at their corresponding altitudes between $60\,\mathrm{km}$ and $100\,\mathrm{km}$ where the line-of-sight tangent of the measurements lies. However, AVKs that represent $\hat{\mathbf{x}}$ above $100\,\mathrm{km}$ peak mostly around $100\,\mathrm{km}$ and their full width at half maximum (FWHM) become much larger. This indicates that the vertical resolutions of these altitudes are lower, which is a direct result of having no measurements at tangent altitudes above $100\,\mathrm{km}$. The retrieval resolution is about $1\text{-}2\,\mathrm{km}$ below $90\,\mathrm{km}$ altitude. Figure 2 also shows the fractional MR. It has a value close to unity between 60 and $100\,\mathrm{km}$ and quickly returning back to zero where no measurements are available. This indicates that the a priori profile has little influence on the estimated result between these altitudes. We use a fractional MR of 0.8 as the threshold to evaluate the quality of the estimated volume emission rate to present the remaining results and perform further analysis in this paper.

Besides MR, OEM also provides us with an analytical expression of the uncertainty in the estimated quantity. The covariance of retrieval noise is

$$\mathbf{S_m} = \mathbf{GS_eG^T}. \tag{14}$$

The diagonal elements of $\mathbf{S_m}$ will be treated as $\mathbf{S_e}$ in Sect. 2.3. The uncertainty of the retrieved volume emission rate, together with the uncertainty of ozone, is presented later.

Figure 3 displays a typical example of the estimated volume emission rate, retrieved along one orbit. Only daytime measurements with a fractional MR greater than 0.8 are shown here. Two airglow layers can clearly be seen, separated by a minimum around $80\,\mathrm{km}$ and mixed with some finer structures between the layers. Figure 3 also shows data gaps in a 'zic-zac' pattern, which are due to the nodding motion of the Odin satellite to facilitate the limb scanning process of the other instruments on-board (OS and SMR). Specifically, in this particular orbit, the satellite was in the so-called 'mesospheric scan mode' which results in data gaps up to $95\,\mathrm{km}$. Hence, not all profiles can reach as low as $60\,\mathrm{km}$, as shown on the right panel of Fig. 3 (e.g. image 915). The first 3-4 nods in Fig. 3 correspond, however, to the 'normal scan mode' resulting in fewer data gaps.

Atmospheric
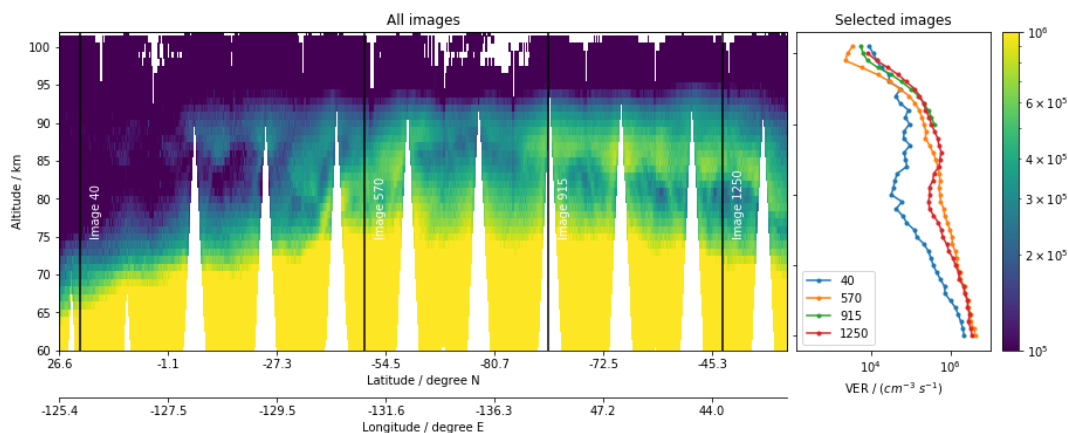Measurement
Techniques
Discussions

Figure 3. Example of retrieved volume emission rate of $O_2(a^1\Delta_g)$ from IRI during daytime for one orbit collected on 2008-1-2, from 15:14:24 to 16:2:31 (orbit number 37400). The panel on the left is a 2D-colour plot, as a function of geographical location and altitude, and the panel on the right is the cross section of the four selected images (along the four black solid lines on the left panel). All results shown here have a measurement response greater than 0.8.

2.3 Retrieval of ozone

Measurements of oxygen IRA band are often used as proxies to estimate daytime ozone concentration because the production of $O_2(a^1\Delta_g)$ is closely linked to the available ozone during the daytime. Measurements such as those from SME, SABER and SCIAMACHY have been used to estimate the ozone concentration using a chemical kinetic model and assuming photochemical

250   equilibrium in a similar fashion (e.g., Thomas et al., 1984; Mlynczak et al., 2007; Zarboo et al., 2018).

 Estimation of ozone concentrations from airglow observation highly relies on the assumption of photochemical equilibrium as well as an accurate chemical kinetic model that relates the volume emission rate to the ozone number density. Reaction processes, Einstein coefficients, reaction rates, photolysis rates, reaction efficiency, solar irradiance, and such must be described as correctly as possible in the chemical model. In the early 1980s, R. J. Thomas et al. (1983) developed a simple photochemical

255   model which only included ozone photolysis in the Hartley band and solar excitation of O_2 in the atmospheric band. This model was applied to SME $O_2(^1\Delta)$ measurements to derive ozone. After that, Mlynczak et al. (1993) showed that the photolysis of O_2 in the Schumann-Runge continuum and Lyman alpha spectral region make significant contributions to the $O_2(a^1\Delta_g)$ production through $O(^1D)$ production at higher altitudes. They concluded that the previous model led to an over-estimation of the ozone concentration from $O_2(a^1\Delta_g)$ observations. Accompanying the launch of SABER, in 2001, this model was further

260   updated, the radiative lifetime of $O_2(a^1\Delta_g)$ was revised and other minor modifications were made, in order to derive ozone profiles from SABER $O_2(a^1\Delta_g)$ measurements (Mlynczak et al., 2007). Yankovsky and Manuilova (2006) have concluded that supplementing the vibrational states in the comprehensive photochemical model helps to get a better agreement between the ozone profiles retrieved from 1.27 μm and 762 nm emissions, based on a numerical experiment on a few METEORS rocket profiles (Mlynczak et al., 2001). Their model includes 3 vibrational levels of $O_2(b^1\Sigma_g^+, v=0,1,2)$, 6 of $O_2(a^1\Delta_g, v=0-5)$ and
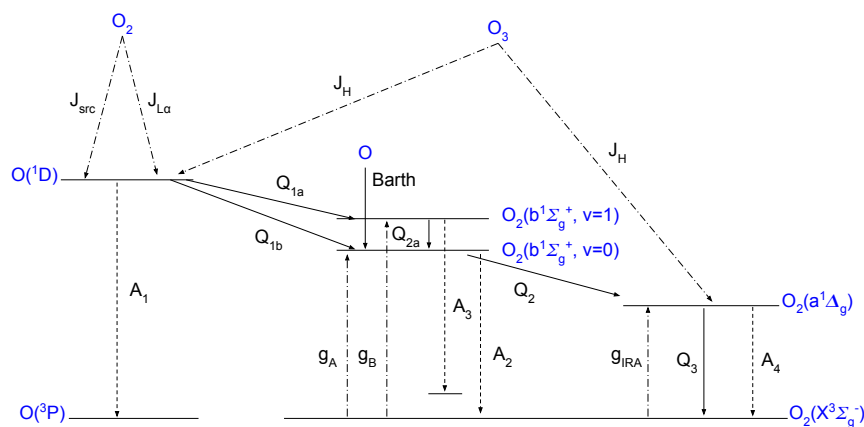
Figure 4. Scheme of kinetics of excited levels of atomic oxygen and molecular oxygen that are used in our model. Detailed reactions are described in Table A1

35 of $O_2(^3\Sigma, v=0-34)$. Yankovsky et al. (2016) have used the same model to simulate how various oxygen airglows perform as proxies for atomic oxygen and ozone.

In this paper, we use a kinetic model with the inclusion of two vibrational levels of $O_2(b^1\Sigma_g^+, v=0,1)$, the Barth-type chemical mechanism (McDade et al., 1986), as well as the solar resonance absorption in the oxygen IRA band itself, which can be described as a model whose the complexity is in between the one used by Mlynczak et al. (1993) and the one used by Yankovsky et al. (2016). Figure 4 illustrates the kinetic scheme of our model. Neglecting most of the vibrational sub-levels of each electronic state should not greatly affect the accuracy of the retrieved ozone. This can be considered as a reasonable assumption, because the population of the electronical-vibrational excited states is mostly dominated by the lowest vibrational state in each electronic level, and these sub-levels are eventually quenched to the lowest vibrational levels as shown by Yankovsky and Manuilova (2006). The processes that we have considered in our kinetic model are listed briefly below, while detailed reactions, as well as the corresponding rate coefficients and quantum yields or efficiencies, can be found in Table A1.

- J_H: photodissociation of ozone in the Hartley band ($\lambda < 310\,\mathrm{nm}$) produces the electronically excited state atomic oxygen $O(^1D)$ and molecular oxygen $O_2(a^1\Delta_g)$;

- $J_{SCR}, J_{L\alpha}$: photodissociation of ground state molecular oxygen in both the Schumann-Runge continuum ($130 \leq \lambda \leq 175\,\mathrm{nm}$) and at Lyman α ($\lambda = 121.6\,\mathrm{nm}$) produces ground state $O(^3P)$ and excited atomic oxygen $O(^1D)$;

- g_A, g_B, g_{IRA}: resonance absorption of ground state molecular oxygen at A-band (762 nm), B-band (688 nm) and oxygen IRA band (1270 nm), respectively;
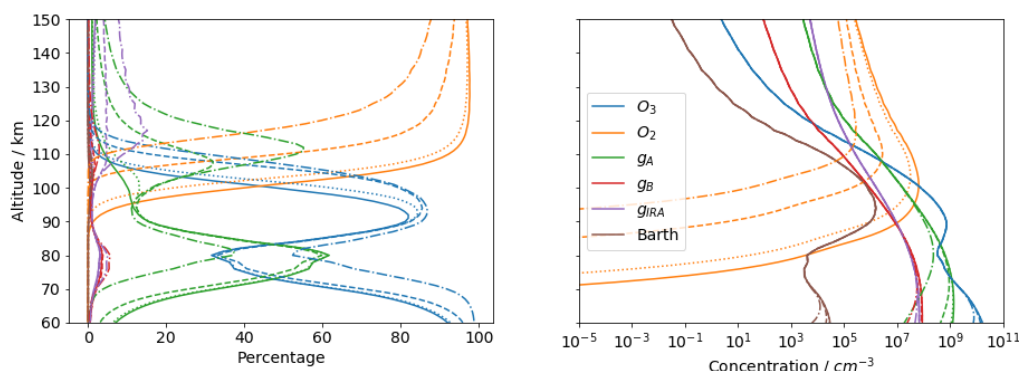
Figure 5. Left panel: relative contributions of 6 different sources to the production rate of $O_2(a^1\Delta_g)$ at 4 solar zenith angles, namely $30°$ (solid lines), $60°$ (dotted lines), $85°$ (dashed lines) and $89.9°$ (dot-dashed lines). Right panel: same as left, but in absolute concentration of $O_2(a^1\Delta_g)$.

- Q_{1a}: transfer of energy by quenching $O(^1D)$ with $O_2(^3\Sigma)$ partly forms ground state atomic oxygen $O(^3P)$ and an excited level of molecular oxygen $O_2(b^1\Sigma_g^+, v=1)$;

285
- Q_{1b}: same as Q_{1a} but to form $O_2(b^1\Sigma_g^+, v=0)$;

- Barth: recombination between two oxygen atoms that through energy transfer processes produce $O_2(b^1\Sigma_g^+)$, known as the Barth-type mechanism;

- Q_{2a}: quenching of $O_2(b^1\Sigma_g^+, v=1)$ to the lower vibrational level $O_2(b^1\Sigma_g^+, v=0)$.

- Q_{2b}: quenching of $O_2(b^1\Sigma_g^+, v=0)$ to the lower electronically excited state of molecular oxygen $O_2(a^1\Delta_g)$;

290
- Q_3: quenching of $O_2(a^1\Delta_g)$ to the ground state $O_2(^3\Sigma)$;

- A_1, A_2, A_3, A_4: the inverse of photochemical lifetime of $O(^1D)$, $O_2(b^1\Sigma_g^+, v=0)$, $O_2(b^1\Sigma_g^+, v=1)$ and $O_2(a^1\Delta_g)$, respectively, when they eventually release their energy as a photon and transfer back to the ground electronic state.

Figure 5 shows the contributions from different production sources to $O_2(a^1\Delta_g)$ in the altitude range 60 to 150 km, both in percentage and absolute concentrations. The simulation is based on a single ozone profile taken from CMAM, a background

295 density and a temperature profile taken from the MSIS climatology (Picone et al., 2002) at different solar zenith angles. Percentage-wise, photodissociation of molecular oxygen in both Schumann-Runge continuum and at Lyman α dominate above 100 km, which is consistent with Mlynczak et al. (1993). Below 100 km $O_2(a^1\Delta_g)$ is mainly produced by photodissociation of ozone in the Hartley band as well as by resonance absorption in the A-band. Resonance absorption in the oxygen B-band and oxygen IRA band contribute as much as 6% at around 80 km or even higher at around 115 km. Moreover, O_2 photodissociation

300 in the altitude range of 60-150 km is highly sensitive to the solar zenith angle while the other photochemical sources are only

sensitive below $90\,\mathrm{km}$ or below. The Barth-type mechanism contributes very little and mainly between $100\text{-}110\,\mathrm{km}$. However, the Barth-type mechanism is the only source during the absence of sunlight since all the other sources involve photochemical reactions, which explains why the nightglow is much weaker than the dayglow (not shown in this paper).

Without simultaneous measurements of $O_2(b^1\Sigma_g^+)$, a reasonable assumption on the efficiency of $O(^1D)$ quenched by
305 ground state O_2 to $O_2(b^1\Sigma_g^+)$ is needed. We assume that 20% are quenched to $O_2(^1\Sigma), v=0$ and that the rest are quenched to $O_2(^1\Sigma), v=1$, as indicated by Yankovsky et al. (2016). All $O_2(^1\Sigma), v=1$ are assumed to be quenched by O_2 and N_2 to $O_2(^1\Sigma), v=0$. Uncertainties in other reaction rate coefficients and their sensitivity to the retrieved ozone concentration are further discussed in Yankovsky et al. (2016).

By assuming photochemical equilibrium for $O(^1D)$, $O_2(b^1\Sigma_g^+)$ and $O_2(a^1\Delta_g)$, one may establish a system of equations
310 to solve for the ozone concentrations from the measured oxygen IRA band volume emission rate. However, it is not straight forward to simply invert the system of equations as the model is non-linear. For example, calculating the solar photolysis rate in the Hartley band and calculating the atomic oxygen density for the Barth-type mechanism depend on how much ozone is present.

We choose to implement the Levenberg-Marquardt algorithm to retrieve the ozone number density iteratively (Rodgers,
315 2000). The ozone number density x at each iteration $n+1$ is derived using the formula

$$\mathbf{x}_{n+1} = \mathbf{x}_n + [(1+\gamma)\mathbf{S_a}^{-1} + \mathbf{K}_n^T\mathbf{S_e}^{-1}\mathbf{K}_n]^{-1}\mathbf{K}_n^T\mathbf{S_e}^{-1}[\mathbf{y} - \mathbf{F}(\mathbf{x}_n)] - \mathbf{S_a}^{-1}[\mathbf{x}_n - \mathbf{x_a}], \tag{15}$$

where γ is the damping parameter and $\mathbf{y}$ is the previously estimated volume emission rate profile (i.e. $\hat{\mathbf{x}}$ in Sect. 2.2) with a measurement response larger than 0.8.

In our implementation, all negative volume emission rates are treated as invalid and replaced by an interpolated value. $\mathbf{F}(\mathbf{x}_n)$
320 is the volume emission rate evaluated by the photochemical model and $\mathbf{K}_n$ is the numerically calculated Jacobian at the n-th iteration based on $\mathbf{F}(\mathbf{x}_n)$. All negative ozone number densities are forced to be $10^{-8}\,\mathrm{cm}^{-3}$ in $\mathbf{F}(\mathbf{x})$. $\mathbf{S_e}$ is a diagonal matrix taken from the retrieval noise of the volume emission rate (i.e. $\mathbf{S_m}$ in Eq. 14). All off-diagonal elements in $\mathbf{S_m}$ are set to zero because the inversion of the full matrix often leads to numerical instability. We use the ozone profiles taken from the CMAM climatology as $\mathbf{x_a}$. $\mathbf{S_a}$ follows the same formula as in the retrieval of volume emission rate (see Eq. 2.2), also with $\sigma_\mathbf{a} = 0.75\mathbf{x_a}$.
325 As the Levenberg-Marquardt method is an iterative procedure to solve non-linear problems, it requires an initial guess. We use $\mathbf{x_a}$ for this. The background air density and temperature are taken from the MSIS climatology. The volume mixing ratio of O_2, N_2 and CO_2 are assumed to be 21%, 78% and $405\,\mathrm{ppm}$, respectively, at all altitudes. For the number density of O, we assume photochemical steady state with ozone.

When iteration has converged, γ is mostly sufficiently small ($\gamma \ll 1$) such that the retrieval can be approximated by using a
330 Gauss-Newton method at the final iteration. Thus the relevant equations for the error analysis are essentially the same as Eq.9 and Eq. 14 described in Sect. 2.2. Similarly, AVK and MR can be assessed using the Jacobian matrix at the final iteration. Finally, the normalized cost of the retrieval is evaluated as

$$\chi_n^2 = [(\mathbf{x}_n - \mathbf{x_a})^T\mathbf{S_a}^{-1}(\mathbf{x}_n - \mathbf{x_a}) + (\mathbf{y} - \mathbf{F}(\mathbf{x}_n))^T\mathbf{S_e}^{-1}(\mathbf{y} - \mathbf{F}(\mathbf{x}_n))]/m \tag{16}$$

where m is the number of elements in $\mathbf{y}$ vector (here is the same as in $\mathbf{x}$ vector, i.e. number of atmospheric layers).

Atmospheric
Measurement
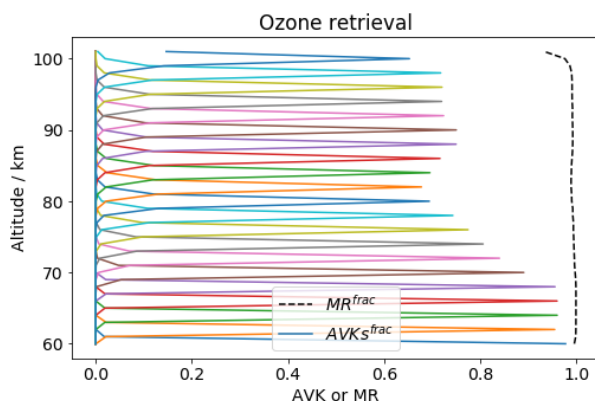Techniques
Discussions

Figure 6. Every two rows of the fractional AVK (solid lines) and MR (black dashed line) from the ozone retrieval of a sample image (the same image as in Fig. 2).
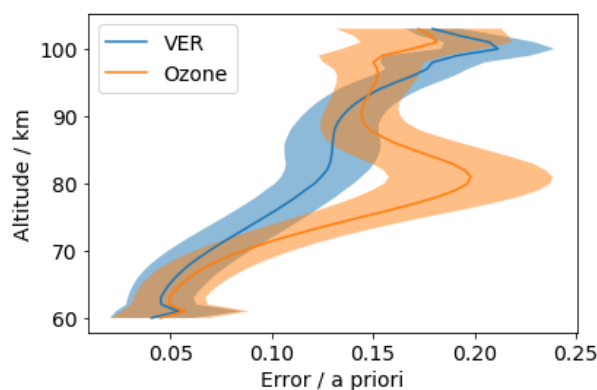

Figure 7. The retrieval noise of the volume emission rate (in blue) and the ozone number density (in orange), scaled with their corresponding a priori profiles. Solid lines are the average profile between Nov 2007 and Oct 2008 and the shaded areas indicate the standard deviation around the averaged uncertainties.

335   An example of the fractional AVK and MR is shown in Fig. 6 indicating that the vertical resolution of the ozone profiles is about 1-2 km. Note that the AVKs above 90 km may not necessarily represent the 'true' values as the retrieval resolution of the oxygen IRA band volume emission rate is not properly taken into account in the ozone retrieval. Thereafter we present our results for all data points that have fractional MR greater than 0.8 and χ^2 smaller than 10. The statistical representation of the uncertainties (i.e. retrieval noise) of both the volume emission rate product and the ozone number density product is presented

340   in Fig. 7, scaled with their a priori profiles. The mean uncertainties on both are around 5-30%, with larger values at higher altitudes where concentrations of $O_2(a^1\Delta_g)$ and ozone are low.

3   Ozone comparisons

To illustrate the performance of the technique described in Sect. 2.1 - Sect. 2.3, daytime ozone profiles have been derived for a test sample of 5 % (every 20th orbits) of all the limb measurements collected by IRI from November 2007 to October 2008. In order to show the fidelity of the results, these IRI ozone profiles are compared with independent datasets derived from OS, SMR, MIPAS and ACE-FTS. We would like to emphasise that a comprehensive validation study is not the primary intention of this study, which will be a valuable future study, after the 20 years data has been processed. We choose to use mainly number density for the comparisons, as it is the natural unit of the IRI and OS ozone profiles. As pointed out by Smith et al. (2013), the differences in background densities to derive ozone VMR introduce additional uncertainty between instruments, we would like to avoid using external data as much as possible. Moreover, the measurements of ozone by SMR at higher altitudes are mostly based on Doppler broadened lines thus the natural unit is closer to number density rather than VMR. Therefore, the visualisation of the profile comparisons in this section is shown in ozone number density, with only one exception in the last panel of Fig. 8.

The datasets considered are briefly described in Sect. 3.1. In Sect. 3.2, we compare coincident observations made by OS, IRI and SMR, all from one example orbit. Since they are on board the same spacecraft, numerous co-incident profiles can be found. Yet, the measurement principles of these three instruments are intrinsically different. The comparison of the zonally averaged daytime ozone profiles from the five aforementioned instruments is discussed in Sect. 3.3. Lastly, in Sect. 3.4, we will focus on the annual cycle of daytime ozone vertical structures in the MLT region. Our goal is to illustrate the consistency of IRI ozone profiles with the other ozone products and, to a lesser extent, to interpret the differences between them.

3.1   Other ozone datasets

Although this is not a complete validation study, independent ozone datasets are used to compare with the new ozone product. The main characteristics of these datasets are given in Table 1. We have selected measurements made between November 2007 and October 2008 by each of the instruments under consideration. A brief description of the measurement principles and data screening methods is provided in this section. More detailed information can be found in the cited publications.

3.1.1   OS

In previous publications, the term OSIRIS ozone product usually refers to the product obtained from the optical grating spectrograph (e.g., McLinden et al., 2007; Bourassa et al., 2018). In Smith et al. (2013), OSIRIS ozone refers to the product derived from the A-band airglow emission by Sheese (2009). In this paper, we will use OS ozone to refer to the product derived from the measured limb scattered sunlight in the Chappuis and Hartley-Huggins bands. These ozone profiles are retrieved from limb radiance pairs and triplets using the multiplicative algebraic reconstruction technique (MART) (Degenstein et al., 2009). This dataset is one of the OSIRIS operational products within the ESA Climate Change Initiative (CCI) programme [2]. Invalid values have already been screened out by the instrument team (Sofieva et al., 2013).

---

[2]ESA CCI programme: http://cci.esa.int/ozone

Atmospheric
Measurement
Techniques
Discussions

Table 1. Main characteristics of the ozone datasets under consideration

Instrument (satellite)	Version	Retrieval uncertainty	Vertical resolution	Vertical coverage	measured quantity
IRI (Odin)	V1-0	5-20 %	1-2 km	60-100 km	ND[a]
OS (Odin)	V5-10	<5 %	2-4 km	10-60 km	ND
SMR (Odin)	V3.0	1 ppmv	2.5-3.5 km	18-65[c] or 20-80[d] km	VMR[b]
MIPAS (Envisat)	V5R	5-10 %	4-8 km	5-100 km	VMR
ACE-FTS (SCISAT-1)	V4	< 3 %	3-4 km	5-95 km	VMR

a: Number density

b: Volume mixing ratio

c: In stratospheric scanning mode

d: In strato-mesospheric scanning mode

3.1.2 SMR

The sub-millimetre radiometer on-board the Odin satellite measures spectra at different altitudes during the limb scans. In particular, it measures the ozone thermal emission line at 545 GHz (this is the so-called frequency mode 2 in the SMR nomenclature). As described in Eriksson (2017), vertical profiles of ozone are retrieved based on the optimal estimation method (OEM) by inverting the radiative transfer equation for a non-scattering atmosphere. This SMR ozone dataset has recently been reprocessed. In this study we use the new ozone main product of SMR, whose quality was assessed in Murtagh et al. (2018). This product is in much better agreement with other instruments, compared to the previous version. All data points that have a measurement response lower than 0.8 are considered as invalid values. Ozone volume mixing ratio (VMR) is provided and the ozone number density is determined by multiplying it with the background number density provided in the dataset. This background number density comes essentially from the combination of ECMWF analyses and the MSIS model. All nighttime measurements (i.e. with the labelled solar zenith angle larger than $90°$) are screened out as we only look at the daytime ozone distribution in this paper.

3.1.3 MIPAS

The Michelson Interferometer for Passive Atmospheric Sounding measures the thermal emission line of ozone at 9.6 µm. We chose to use the middle atmospheric mode in our analysis. This dataset has been processed by KIT-IMK and documented in Van Der A et al. (2017); López-Puertas et al. (2018). As for SMR, all nighttime measurements are excluded from further analysis. Following the MIPAS level 2 screening recommendations, all data points that are flagged by 'visibility = 0' or have an averaging kernel diagonal element of less than 0.03 are not considered. Ozone concentration is given in VMR. We use the temperature and pressure measured by MIPAS to calculate the ozone number density.

3.1.4 ACE-FTS

The Fourier Transform Spectrometer on the Atmospheric Chemistry Experiment measures ozone along with temperature and pressure profiles by using the solar occultation measurement technique (Bernath et al., 2005). In contrast to measuring scattered sunlight such as done by OS, ACE-FTS aims at the sun directly through the limb and can therefore only measure a maximum of two profiles per orbit, greatly limiting the sampling frequency compared to the other instruments. The retrieval method is described by Boone et al. (2005). Ozone concentration is given in VMR. We use the measured temperature and pressure to calculate ozone number density. Following the version 4 data screening recommendations, all data points that are flagged '-999' and '-888' are filtered out. In addition, data points associated with a statistical error for ozone VMR larger than 2 ppm are not considered in our analysis.

3.2 Coincident comparison

As mentioned in the earlier sections, the Odin satellite collects ozone profiles from three independent instruments. SMR measures thermal emission of an excited state of ozone in the microwave region at 545 GHz, OS measures scattered solar light in the Hartley-Huggins and Chapuis bands and IRI measures the oxygen airglow emission at oxygen IRA band. Due to the underlying measurement principles of these datasets, the altitude ranges and parts of the orbit during which data is available vary. This is depicted in Fig. 8. For this particular example orbit, SMR ozone measures from 10 to a maximum 80 km altitude both daytime and nighttime throughout the orbit, while OS measures ozone only up to 55 km and during only half of the orbit, where scattered sunlight is available. IRI ozone covers the altitude range from 60 to 100 km as limited by the VER retrieval grid and measurement response (see sections 2.2 and 2.3). IRI ozone is also limited to the day part of the orbit since the oxygen airglow primarily relies on photochemical reactions, as discussed in Sect. 2.3.

It is worth mentioning that Fig. 8 also illustrates the high sampling rate of IRI, over 70 times higher than SMR and OS due to the imaging sensor. The bottom left panel of Fig. 8 shows a single ozone density profile collected at the same time and location by all three instruments. The volume mixing ratio of IRI ozone is derived based on the background density included in the SMR product (see Sect. 3.1.2) and is shown in the bottom right panel of Fig. 8. Both the primary and secondary ozone layers appear clearly in the plots. These two plots suggest that these coincident ozone profiles would merge smoothly with each other, even though they do not cover the same altitude ranges. This result shows how consistent the ozone observations from these three instruments aboard Odin are with each other, despite the fact that they use intrinsically different measurement techniques. However, if one meticulously studies the 2D-colour plot of the IRI ozone in the mid-panel of Fig. 8, some vertical stripes may appear following the scanning pattern. This effect is probably a result of the stray light correction process in the level 1 data (See Sect. 2.1).

3.3 Zonal average comparison

Figure 9 depicts one example month of ozone distribution in number density for the five different instruments, averaged in 10 ° latitude bins (upper panels) and the corresponding profile count in each latitude bin (lower panels). In this case, December
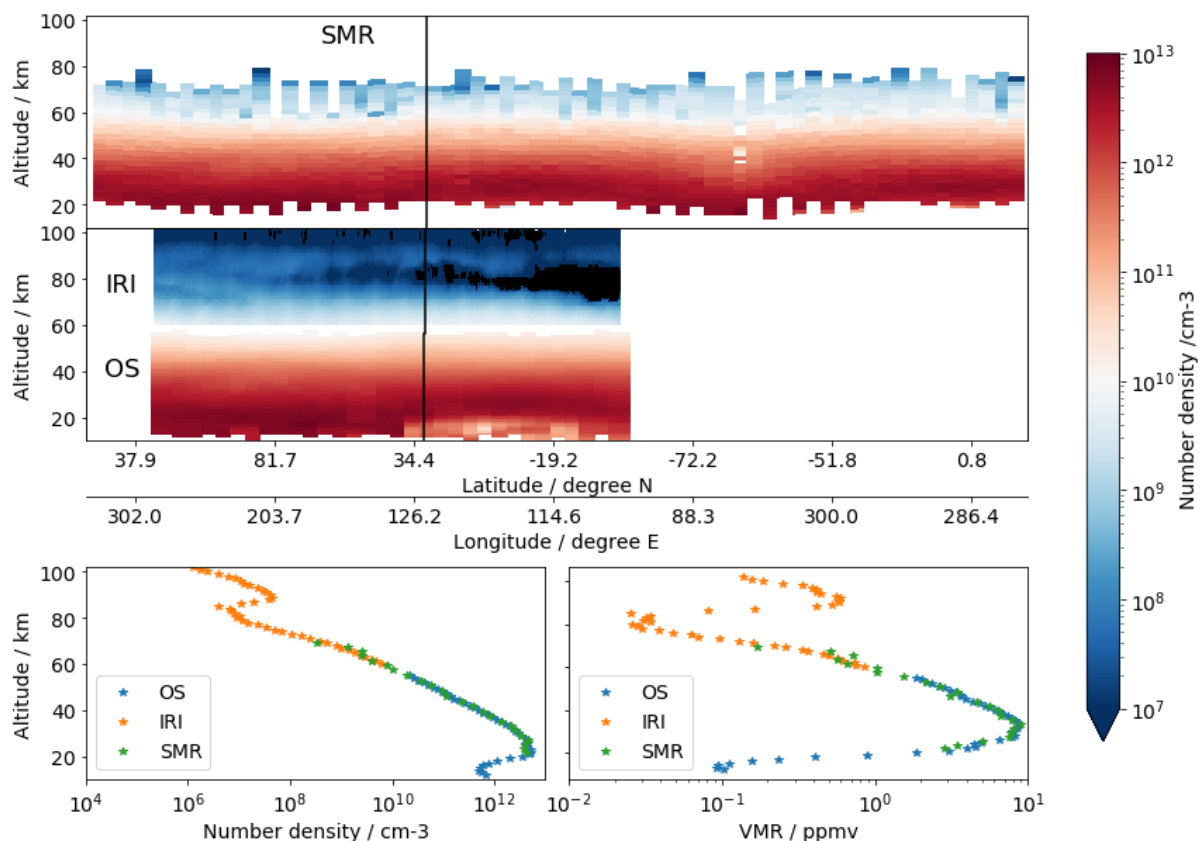
Atmospheric
Measurement
Techniques
Open Access
EGU
Discussions

Figure 8. Upper panel: 2D-colour plot of SMR ozone number density profiles for one orbit as function of altitude and geographical location, collected on 2008-3-30 from 22:14:56 to 23:51:03 (Odin orbit number 38720). Middle panel: 2D-colour plot of IRI (above 60 km) and OS (below 60 km) daytime ozone profiles in the same orbit as SMR. Black colour indicates that the estimated ozone value is negative. Bottom left: ozone number density profiles from the scan/image of OS, IRI and SMR indicated by the black vertical line in the panels above. Bottom right: same as the bottom left panel but volume mixing ratio in ppmv.

2007 is shown. Although the vertical coverage of individual profile may differ, IRI shows a great advantage with a significantly
425   higher sampling rate than the other instruments. Note that only every 20th orbits of IRI measurements have been processed in
this study. Once all orbits are processed, the number of profiles will be roughly 20 times higher. The latitudinal distribution
of the stratospheric main ozone layer (below 60 km) is in overall good agreement between OS, SMR, ACE-FTS and MIPAS,
where ozone peaks at a higher altitude in the equatorial region and lower in polar regions, nearly symmetric with respect to the
equator.
430   In the MLT region (above 60 km), the latitudinal distribution and the strength of the secondary ozone maximum seem to
be less consistent among IRI, SMR, ACE-FTS and MIPAS. IRI observes a deep ozone trough (i.e. the minimum separating
the two ozone layers) concentrated in the mid-high latitude towards the winter pole centred at 75 km. The ozone trough is so
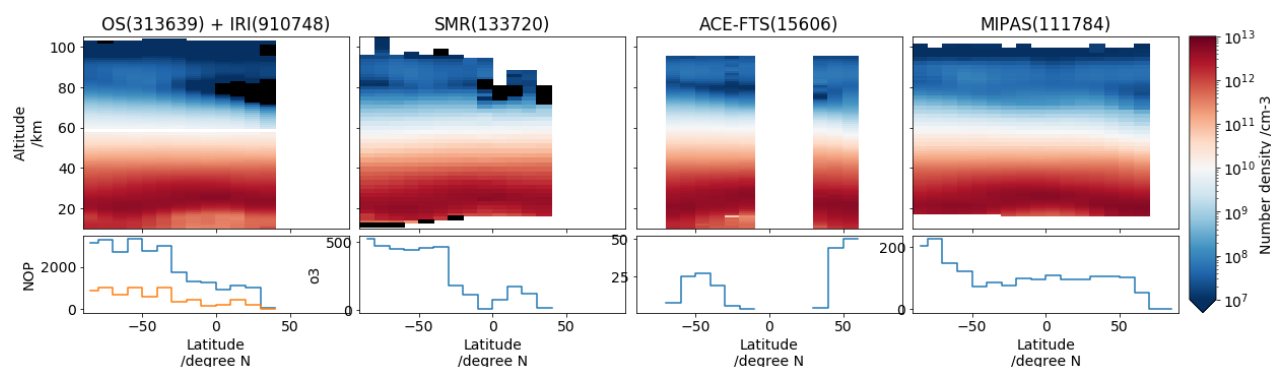
Figure 9. Zonal average ozone number density observed in December 2007, with $10°$ latitude bins. The first 2D-colour plot contains data from two instruments, with OS below $59\,\mathrm{km}$ and IRI above $60\,\mathrm{km}$. The second to fourth 2D-colour plots correspond to SMR, ACE-FTS and MIPAS, respectively. The numbers in brackets, indicated in the titles, are the total number of samples (profiles) that are available within the month under consideration. Black colour indicates negative ozone value. Bottom panels correspond to histograms showing the number of profiles that are accounted for the zonal averages. Note that the scales of the vertical axes are different in the bottom panels.

deep that the estimated values can include negative values due to the weak volume emission rate and measurement uncertainty and therefore blanked out in Fig. 9. SMR observations agree well with IRI, with the ozone trough in the northern hemisphere

435   so deep that the measured signal is too weak to give valid data. ACE-FTS, however, observes a deeper ozone trough in the summer hemisphere than IRI, while comparison in the winter hemisphere is not possible due to lacking overlapping data. MIPAS observes a deeper trough in the winter hemisphere as in IRI and SMR data, but a relatively even distribution in the MLT region. Nevertheless, all of these instruments display an ozone trough lower in altitude towards the winter pole. This latitudinal asymmetry may be the result of the pole-to-pole meridional circulation. The asymmetric pattern of the ozone trough

440   follows an annual cycle which can be studied in Fig. 12 more easily.

One must be cautious when looking at such a zonal average comparison. Ozone production and loss rates depend on solar zenith angle (SZA), and their dependency varies with altitude. Especially in the MLT region, the ozone concentration changes drastically at sunrise and sunset (Allen et al., 1984; Huang et al., 2008), (see also the diurnal variation of ozone estimated from the NCAR ROSE model in Kyrölä et al. (2010) their Fig. 8). The sampling patterns of the three satellite platforms considered

445   in this paper are shown in Fig. 10. OS, IRI and SMR orbit the Earth close to the day-night terminator with SZA in the range 60-90$°$ with the lower angles towards the summer pole. ACE samples exactly at sunrise and sunset, while MIPAS samples at SZA between 22 and 90$°$ with the lower angles around the equatorial region and higher angles in the polar regions. It is also worth mentioning that the number of observations can differ by several orders of magnitude in each latitude and altitude bin, as seen in the lower panels of Fig. 9. As mentioned in Sofieva et al. (2014), insufficient or inhomogeneous sampling can result in

450   inaccurate average estimates. However, a complete investigation of the sampling uncertainty is beyond the scope of this paper.

For a more detailed comparison, a single latitude bin is selected and the ozone number density measured by the five instruments are depicted in Fig. 11 (left panel). The zonal mean profiles agree well with each other below $60\,\mathrm{km}$. Regarding the
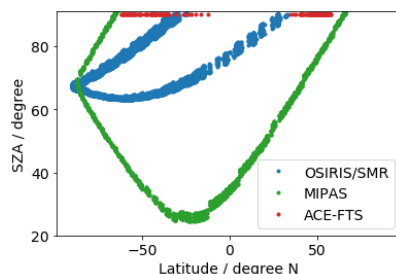
Figure 10. The sampling patterns of the instruments on three spacecrafts with respect to the local solar zenith angle (SZA) during December 2007, as function of latitude.
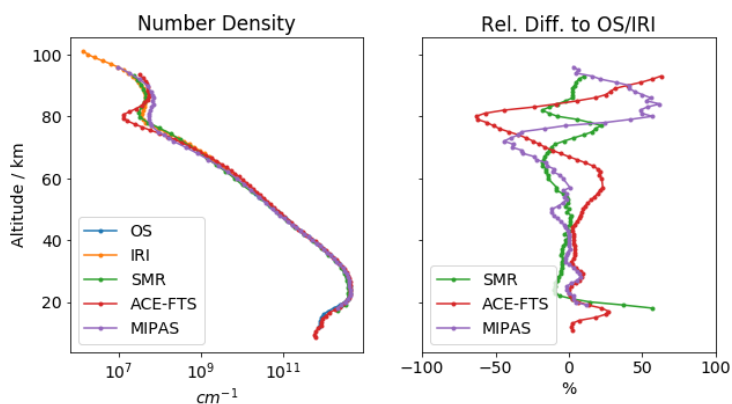

Figure 11. A comparison of zonal mean profiles between the five instruments for a selected latitude bin $(30 - 40° S)$ in December 2007. The left panel shows the absolute comparison in number density and the right panel shows the relative difference to the OS and IRI zonal mean profiles.

mesospheric data, there is good agreement on the average magnitude of the secondary maximum located at $90\,km$. However, the depth of the ozone trough differs between these ozone datasets. Figure 11 also depict the relative differences (right panel)

455 to the OS (below $60\,km$) or IRI (above $60\,km$) zonal mean profile. SMR agrees relatively well with IRI with a maximum of 20% difference around the ozone trough region. MIPAS exhibits a difference of maximum 50% relative to IRI since the height of the secondary layer is slightly off-set. The disagreement of MIPAS would probably be better if we would take into account the vertical resolution correctly of all the instruments. ACE-FTS appears to have as large as 70% difference at the minimum (around $80\,km$) and at the top of the secondary ozone layer (above $95\,km$). These differences are expected since the ozone

460 density at the trough and above the peak is so low that relative uncertainties become very large.

Atmospheric
Measurement
Techniques
Discussions

3.4 Monthly mean time series comparison

In this section, we focus on ozone comparison in the MLT region. As can be seen in Fig. 9, OS rarely collects ozone profiles in the region where IRI measures. We will therefore only look at the ozone number density from four instruments: IRI, SMR, ACE-FTS and MIPAS.

465   Figure 12 shows the monthly mean ozone number density in the MLT region for three latitude bands: 30-50 °N, 10 °S-10 °N and 30-50 °S. It is noticeable that for IRI, SMR and ACE-FTS the top of the stratospheric ozone layer at mid-latitudes extends to a higher altitude in the summer months, while MIPAS tends to show higher altitudes in spring and autumn. At mid-latitudes, both IRI and SMR consistently depict a stronger secondary maximum in summer and deeper trough in winter, the same can be seen in MIPAS even though it is less pronounced. MIPAS observations of ozone density show relatively small temporal

470   and spatial variation. These differences may be the result of the lower vertical resolution of MIPAS. ACE-FTS samples ozone profiles at a much lower rate that is not sufficient to produce a continuous time series, thus we show a discreet 2D plot instead of contour plot in Fig. 12. A stronger seasonal variation in the mid-latitude bands is also observed by ACE-FTS, with a deeper trough at the end of spring and beginning of autumn. Unlike the others, the spatial and temporal variation of the secondary maximum is not so obvious for ACE-FTS due to the low sampling rate. Overall, IRI agrees very well with SMR, and, to a

475   lesser extent, with MIPAS. All of the instruments display a somewhat weaker secondary maximum in the equatorial region than in mid-latitude regions, which is also shown by Smith et al. (2013) in their Fig. 13.

The differences between IRI, ACE-FTS and MIPAS in Fig.12 may be explained by their sampling at different SZA and the underlying assumptions in their retrieval techniques. IRI and SMR sample at the same SZA all the time, with lower SZA in the summer months in the mid-latitude belts and rather constant SZA in the equatorial belt. In general MIPAS samples at a

480   lower SZA than IRI and SMR, which will affect the represented mean in the MLT region where the diurnal variation is strong. Regardless of the location and season, ACE-FTS is always sampling at SZA of 90 °, when ozone density experiences a rapid change in the MLT region. Thus such a monthly mean profile should be treated with caution since it may not necessarily well represent the spatial and temporal distribution of daytime ozone.

4   Conclusions

485   In this study, we present a new high along-track resolution IRA band and ozone dataset. We first briefly presented the updated calibration scheme that is used on the OSIRIS IR imager level 1 data. From the limb radiance measurements, an optimal estimation method is used to retrieve the volume emission rate of $O_2(a^1\Delta_g)$ image by image. The implementation of the inversion includes a simple linear forward model that only considers emission in the radiative transfer equation. An example orbit of the dayglow volume emission rate shows a clear structure of a main layer and a secondary maximum, accompanied by

490   some finer structures. The nodding motion of the satellite occasionally 'creates' data gaps through the airglow layers.

Once the volume emission rate of $O_2(a^1\Delta_g)$ is retrieved, ozone is derived based on the non-linear inversion of a photo-chemical kinetic model that describes the relationship between ozone and $O_2(a^1\Delta_g)$. The kinetic model is a slightly extended version of the one developed by Mlynczak et al. (1993), which includes mechanisms such as photo-dissociation of O_2 and O_3,
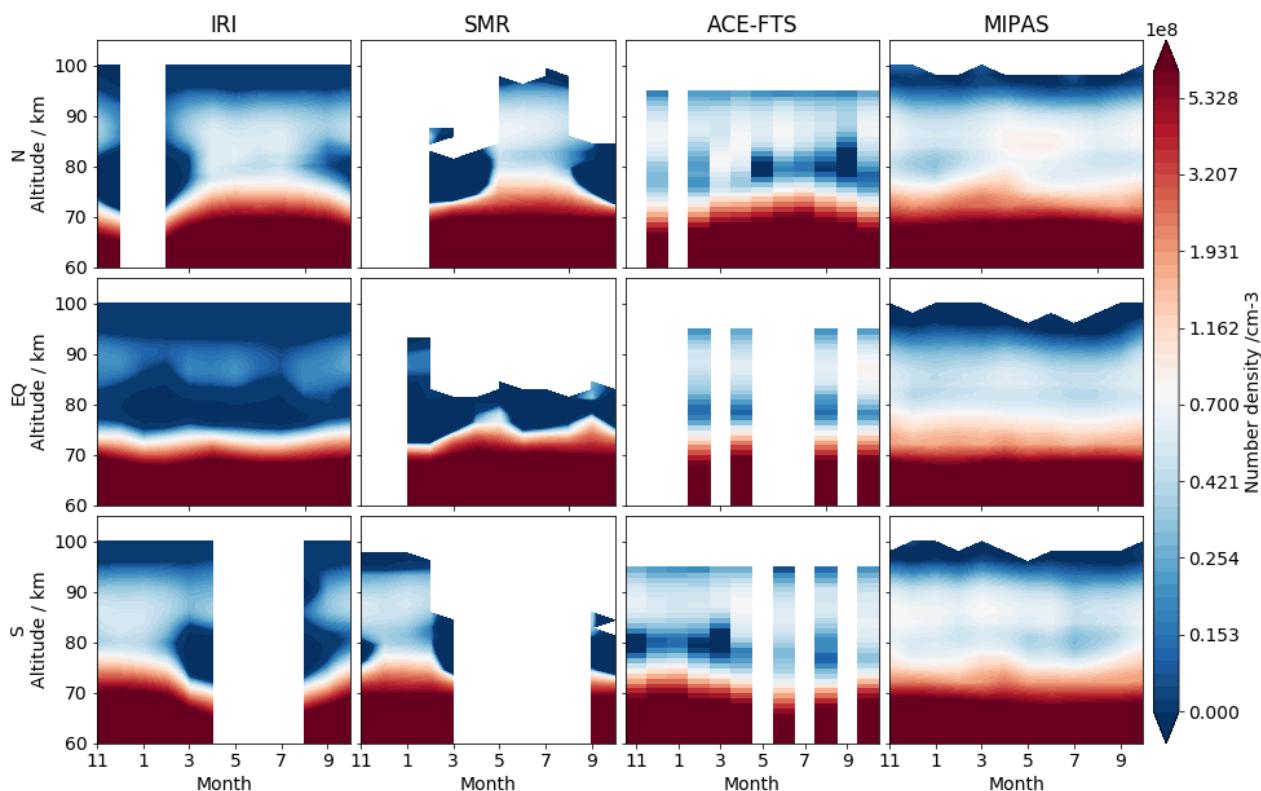
Figure 12. Monthly mean ozone number density from November 2007 to October 2008, in three latitude bands: 30-50 °N (first row), 10 °S-10 °N (second row) and 30-50 °S (third row). Columns from the left to right represent IRI, SMR, ACE-FTS and MIPAS, respectively.

solar excitation of O_2 and quenching of different excited stated of atomic and molecular oxygen. The inversion is based on the

495   implementation of the Levenberg-Marquardt algorithm.

Finally, the daytime ozone density retrieved from a test sample of IRI measurements made between November 2007 and October 2008 is compared to the ozone products collected from external instruments, namely SMR, OS, MIPAS and ACE-FTS. The comparison of the coincident profiles of IRI, OS and SMR of an arbitrarily selected orbit showed that they merge rather well, although they do not measure over the same altitude ranges. The comparison also demonstrates the advantage of the high

500   sampling rate of IRI. Zonally averaged profiles give us an overall image of the inferred global distribution of ozone. It can be seen that the ozone trough in the MLT is deeper and at lower altitude in the winter hemisphere which is consistent between IRI, SMR, and MIPAS. One year of monthly mean profiles separated into three latitudinal bands depict a clear seasonal pattern in IRI and SMR, with a stronger secondary maximum in the summer months and deeper ozone trough in the winter months especially at mid-latitudes. MIPAS monthly mean ozone also shows a similar annual cycle, but less pronounced. A possible

505   explanation of differences between instruments may come from the sampling pattern of the local sun zenith angle and the underlying assumptions in their ozone retrievals such as vertical resolution.

Atmospheric
Measurement
Techniques
Discussions

Overall, this study has demonstrated the technique of retrieving ozone density from the $O_2(a^1\Delta_g)$ limb radiance measurements by IRI. The inter-comparisons with the other independent ozone datasets shows that such a technique can be further applied to all IRI limb radiance data throughout the 19 years of the mission to date, leading to a new, long-term, high resolution
510 ozone dataset in the middle atmosphere.

Data availability. The data will be available on our ftp server odin-osiris.usask.ca by special request. More information is available at https://research-groups.usask.ca/osiris/

Appendix A: Appended tables

Atmospheric
Measurement
Techniques

Open Access

EGU

Discussions

Table A1. Reactions and their coefficients included in the photochemical model

Symbol in Fig.4	Reaction	Rate coefficient (in molecule cm s units)	Efficiency	Reference
J_H	$O_3 + h\nu \rightarrow O_2(a^1\Delta_g) + O(^1D)$	Vertical profile	0.9	JPL
J_{src}	$O_2 + h\nu \rightarrow O(^3P) + O(^1D)$	Vertical profile		JPL
$J_{L\alpha}$	$O_2 + h\nu \rightarrow O(^3P) + O(^1D)$	Vertical profile	0.44	JPL
g_A	$O_2 + h\nu \rightarrow O_2(b^1\Sigma_g^+, v=0)$	Vertical profile		HITRAN
g_B	$O_2 + h\nu \rightarrow O_2(b^1\Sigma_g^+, v=1)$	Vertical profile		HITRAN
g_{IRA}	$O_2 + h\nu \rightarrow O_2(a^1\Delta_g)$	Vertical profile		HITRAN
A_1	$O(^1D) \rightarrow O + h\nu(\lambda=630\,\text{nm})$	6.81×10^{-3}		a
A_2	$O_2(b^1\Sigma_g^+, v=0) \rightarrow O_2 + h\nu(\lambda=762\,\text{nm})$	8.34×10^{-2}		a
A_3	$O_2(b^1\Sigma_g^+, v=1) \rightarrow O_2(b^1\Sigma_g^+, v=1) + h\nu(\lambda=771\,\text{nm})$	7.2×10^{-2}		a
A_4	$O_2(a^1\Delta_g) \rightarrow O_2 + h\nu(\lambda=1.24\,\mu\text{m})$	2.26×10^{-4}		a
Q_1	$O(^1D) + N_2 \rightarrow O(^3P) + N_2$	$2.15 \times 10^{-11} \times \exp(-110/T)$		JPL
Q_{1a}	$O(^1D) + O_2 \rightarrow O(^3P) + O_2(b^1\Sigma_g^+, v=1)$	$3.3 \times 10^{-11} \times \exp(-55/T)$	0.8	JPL, a
Q_{1b}	$O(^1D) + O_2 \rightarrow O(^3P) + O_2(b^1\Sigma_g^+, v=0)$	$3.3 \times 10^{-11} \times \exp(-55/T)$	0.2	JPL, a
Q_{2a}	$O_2(b^1\Sigma_g^+, v=1) + O_2$ $\rightarrow O_2(X^3\Sigma_g^-, v=1) + O_2(b^1\Sigma_g^+, v=0)$	$2.2 \times 10^{-11} \times \exp(-115/T)$		a
Q_{2a}	$O_2(b^1\Sigma_g^+, v=1) + O(^3P) \rightarrow O_2 + O(^3P)$	4.5×10^{-12}		a
Q_{2a}	$O_2(b^1\Sigma_g^+, v=1) + O_3 \rightarrow 2O_2 + O(^3P)$	3×10^{-10}		a
Q_{2a}	$O_2(b^1\Sigma_g^+, v=1) + N_2 \rightarrow N_2 + O_2(b^1\Sigma_g^+, v=0)$	7×10^{-13}		a
Q_{2b}	$O_2(b^1\Sigma_g^+, v=0) + N_2 \rightarrow O_2(a^1\Delta_g) + N_2$	2.1×10^{-15}		JPL
Q_{2b}	$O_2(b^1\Sigma_g^+, v=0) + O_2 \rightarrow O_2(a^1\Delta_g) + O_2$	3.9×10^{-17}		JPL
Q_{2b}	$O_2(b^1\Sigma_g^+, v=0) + O \rightarrow O_2(a^1\Delta_g) + O$	8×10^{-14}		JPL
Q_{2b}	$O_2(b^1\Sigma_g^+, v=0) + O_3 \rightarrow O_2(a^1\Delta_g) + O_3$	2.2×10^{-11}		JPL
Q_{2b}	$O_2(b^1\Sigma_g^+, v=0) + CO_2 \rightarrow O_2(a^1\Delta_g) + CO_2$	4.2×10^{-13}		JPL
Q_3	$O_2(a^1\Delta_g) + O_2 \rightarrow 2O_2$	$3.6 \times 10^{-18} \times \exp(-220/T)$		JPL
Q_3	$O_2(a^1\Delta_g) + N_2 \rightarrow O_2 + N_2$	1×10^{-20}		JPL
Q_3	$O_2(a^1\Delta_g) + O \rightarrow O_2 + O$	2×10^{-16}		JPL
Q_3	$O_2(a^1\Delta_g) + O_3 \rightarrow O_2 + O_3$	$5.2 \times 10^{-11} \times \exp(2840/T)$		JPL
Barth	$2O + M \rightarrow O_2^* + M$	$4.7 \times 10^{-33} \times \exp(300/T)$	see footnote	b
Barth	$O_2^* + O, O_2, N_2 \rightarrow \text{allproducts}$	see footnote		b
Barth	$O_2^* + O_2 \rightarrow O_2 + O_2(b^1\Sigma_g^+)$	see footnote	see footnote	b

a: See reference list in Yankovsky et al. (2016)

b: Empirical quenching coefficients are introduced. In accordance with notation in McDade et al. (1986), $C^{O_2} = 6.6$, $C^O = 19$

JPL: See reference list in the JPL Publication 10-10 (Burkholder et al., 2015)

HITRAN: Gordon et al. (2017)

Table A2. A list of acronyms that has been used in the paper

Acronym	Full spelling
HALOE	Halogen Occultation Experiment
ACE-FTS	tmospheric Chemistry Experiment - Fourier Transform Spectrometer
SOFIE	Solar Occultation for Ice Experiment
GOMOS	Global Ozone Monitoring by Occultation of Stars
SABER	Sounding of the Atmosphere using Broadband Emission Radiometry
MIPAS	Michelson Interferometer for Passive Atmospheric Sounding
SMR	Sub-Millimetre Radiometer
SME	Solar Mesosphere Explorer
SCIAMACHY	SCanning Imaging Absorption SpectroMeter for Atmospheric CHartographY
OS	Optical Spectrograph
IRI	Infrared Imager
OSIRIS	Optical Spectrograph and InfraRed Imaging System
METEORS	Mesosphere-Thermosphere Emissions for Ozone Remote Sensing
MLT	Mesosphere and lower thermosphere
OEM	Optimal estimation method
MAP	Maximum a posteriori
AVK	Averaging kernel
MR	Measurement response
FWHM	Full Width Half Maximum
SZA	Solar zenith angle
CMAM	Canadian Middle Atmosphere Model
MSIS	Mass Spectrometer Incoherent Scatter
ECMWF	European Centre for Medium-Range Weather Forecasts
VMR	Volume mixing ratio
IRA band	InfraRed Atmospheric band
A band	Atmospheric band

Atmospheric
Measurement
Techniques
Discussions

520

Atmospheric
Measurement
Techniques
Discussions

References

Allen, M., Lunine, J. I., and Yung, Y. L.: The Vertical Distribution of Ozone in the Mesosphere and Lower Thermosphere, Tech. Rep. D3, 1984.

525 Baron, P., Ricaud, P., Noë, J. d. l., Eriksson, J. E. P., Merino, F., Ridal, M., and Murtagh, D. P.: Studies for the Odin sub-millimetre radiometer. II. Retrieval methodology, Canadian Journal of Physics, 80, 341–356, https://doi.org/10.1139/p01-150, https://doi.org/10.1139/p01-150, 2002.

Bernath, P. F., McElroy, C. T., Abrams, M. C., Boone, C. D., Butler, M., Camy-Peyret, C., Carleer, M., Clerbaux, C., Coheur, P. F., Colin, R., DeCola, P., DeMazière, M., Drummond, J. R., Dufour, D., Evans, W. F., Fast, H., Fussen, D., Gilbert, K., Jennings, D. E., Llewellyn, E. J.,
530 Lowe, R. P., Mahieu, E., McConnell, J. C., McHugh, M., McLeod, S. D., Michaud, R., Midwinter, C., Nassar, R., Nichitiu, F., Nowlan, C., Rinsland, C. P., Rochon, Y. J., Rowlands, N., Semeniuk, K., Simon, P., Skelton, R., Sloan, J. J., Soucy, M. A., Strong, K., Tremblay, P., Turnbull, D., Walker, K. A., Walkty, I., Wardle, D. A., Wehrle, V., Zander, R., and Zou, J.: Atmospheric chemistry experiment (ACE): Mission overview, https://doi.org/10.1029/2005GL022386, 2005.

Boone, C. D., Nassar, R., Walker, K. A., Rochon, Y., Mcleod, S. D., Rinsland, C. P., and Bernath, P. F.: Retrievals for the atmospheric
535 chemistry experiment Fourier-transform spectrometer, Tech. rep., 2005.

Bourassa, A.: The characterization and calibration of the OSIRIS infrared imager, Master's thesis, 2003.

Bourassa, A. E., Roth, C. Z., Zawada, D. J., Rieger, L. A., McLinden, C. A., and Degenstein, D. A.: Drift-corrected Odin-OSIRIS ozone product: Algorithm and updated stratospheric ozone trends, Atmospheric Measurement Techniques, 11, 489–498, https://doi.org/10.5194/amt-11-489-2018, 2018.

540 Brasseur, G. and Solomon, S.: Aeronomy of the Middle Atmosphere, vol. 53, https://doi.org/10.1017/CBO9781107415324.004, 2005.

Burkholder, J. B., Sander, S. P., Abbatt, J. P. D., Barker, J. R., Huie, R. E., Kolb, C. E., Kurylo, M. J., Orkin, V. L., Wilmouth, D. M., and Wine, P. H.: Chemical Kinetics and Photochemical Data for Use in Atmospheric Studies Evaluation Number 18 NASA Panel for Data Evaluation, Tech. rep., http://jpldataeval.jpl.nasa.gov/, 2015.

Chapman, S.: On ozone and atomic oxygen in the upper atmosphere, Philosophical Magazine and Journal of Science, 10, 369–383,
545 https://doi.org/10.1080/14786443009461588, 1930.

Degenstein, D.: Atmospheric volume emission tomography from a satellite platform, Ph.D. thesis, Saskatoon, 1999.

Degenstein, D. A., Llewellyn, E. J., and Lloyd, N. D.: Tomographic retrieval of the oxygen infrared atmospheric band with the OSIRIS infrared imager, Canadian Journal of Physics, 82, 501–515, https://doi.org/10.1139/p04-024, 2004.

Degenstein, D. A., Gattinger, R. L., Lloyd, N. D., Bourassa, A. E., Wiensz, J. T., and Llewellyn, E. J.: Observations
550 of an extended mesospheric tertiary ozone peak, Journal of Atmospheric and Solar-Terrestrial Physics, 67, 1395–1402, https://doi.org/10.1016/j.jastp.2005.06.019, 2005a.

Degenstein, D. A., Lloyd, N. D., Bourassa, A. E., Gattinger, R. L., and Llewellyn, E. J.: Observations of mesospheric ozone depletion during the October 28, 2003 solar proton event OSIRIS, Geophysical Research Letters, 32, 1–4, https://doi.org/10.1029/2004GL021521, 2005b.

Degenstein, D. A., Bourassa, A. E., Roth, C. Z., and Llewellyn, E. J.: Limb scatter ozone retrieval from 10 to 60 km using a multiplicative
555 algebraic reconstruction technique, Tech. rep., www.atmos-chem-phys.net/9/6521/2009/, 2009.

Eriksson, P.: Algorithm Theoretical Basis Document-Level 2 processing, Tech. rep., https://odin.rss.chalmers.se/static/documents/L1_ATBD. pdf, 2017.

Gordon, I. E., Rothman, L. S., Hill, C., Kochanov, R. V., Tan, Y., Bernath, P. F., Birk, M., Boudon, V., Campargue, A., Chance, K. V., Drouin,
B. J., Flaud, J. M., Gamache, R. R., Hodges, J. T., Jacquemart, D., Perevalov, V. I., Perrin, A., Shine, K. P., Smith, M. A., Tennyson, J.,
560   Toon, G. C., Tran, H., Tyuterev, V. G., Barbe, A., Császár, A. G., Devi, V. M., Furtenbacher, T., Harrison, J. J., Hartmann, J. M., Jolly, A.,
Johnson, T. J., Karman, T., Kleiner, I., Kyuberis, A. A., Loos, J., Lyulin, O. M., Massie, S. T., Mikhailenko, S. N., Moazzen-Ahmadi, N.,
Müller, H. S., Naumenko, O. V., Nikitin, A. V., Polyansky, O. L., Rey, M., Rotger, M., Sharpe, S. W., Sung, K., Starikova, E., Tashkun,
S. A., Auwera, J. V., Wagner, G., Wilzewski, J., Wcisło, P., Yu, S., and Zak, E. J.: The HITRAN2016 molecular spectroscopic database,
Journal of Quantitative Spectroscopy and Radiative Transfer, 203, 3–69, https://doi.org/10.1016/j.jqsrt.2017.06.038, 2017.
565   Hartogh, P., Jarchow, C., Sonnemann, G. R., and Grygalashvyly, M.: On the spatiotemporal behavior of ozone within the up-
per mesosphere/mesopause region under nearly polar night conditions, Journal of Geophysical Research Atmospheres, 109,
https://doi.org/10.1029/2004JD004576, 2004.
Hays, P. B. and Roble, R. G.: Observation of mesospheric ozone at low latitudes, Planetary and Space Science, 21, 273–279,
https://doi.org/https://doi.org/10.1016/0032-0633(73)90011-1, 1973.
570   Hoffmann, C. G., Raffalski, U., Palm, M., Funke, B., Golchert, S. H., Hochschild, G., and Notholt, J.: Observation of strato-mesospheric CO
above Kiruna with ground-based microwave radiometry - Retrieval and satellite comparison, Atmospheric Measurement Techniques, 4,
2389–2408, https://doi.org/10.5194/amt-4-2389-2011, 2011.
Huang, F. T., Mayr, H. G., Russell, J. M., Mlynczak, M. G., and Reber, C. A.: Ozone diurnal variations and mean profiles in the mesosphere,
lower thermosphere, and stratosphere, based on measurements from SABER on TIMED, Journal of Geophysical Research: Space Physics,
575   113, https://doi.org/10.1029/2007JA012739, 2008.
Ivanov, E.: Computer Modeling of the OSIRIS Infrared Imager, Master's thesis, University of Saskatchewan, 2000.
Kyrölä, E., Tamminen, J., Sofieva, V., Bertaux, J. L., Hauchecorne, A., Dalaudier, F., Fussen, D., Vanhellemont, F., Fanton D'Andon, O.,
Barrot, G., Guirlet, M., Fehr, T., and Saavedra De Miguel, L.: GOMOS O3, NO2, and NO3 observations in 2002-2008, Atmospheric
Chemistry and Physics, 10, 7723–7738, https://doi.org/10.5194/acp-10-7723-2010, 2010.
580   Llewellyn, E. J., Lloyd, N. D., Degenstein, D. A., Gattinger, R. L., Petelina, S. V., Bourassa, A. E., Wiensz, J. T., Ivanov, E. V., McDade,
I. C., Solheim, B. H., McConnell, J. C., Haley, C. S., von Savigny, C., Sioris, C. E., McLinden, C. A., Griffioen, E., Kaminski, J., Evans,
W. F. J., Puckrin, E., Strong, K., Wehrle, V., Hum, R. H., Kendall, D. J. W., Matsushita, J., Murtagh, D. P., Brohede, S., Stegman, J., Witt,
G., Barnes, G., Payne, W. F., Piché, L., Smith, K., Warshaw, G., Deslauniers, D. L., Marchand, P., Richardson, E. H., King, R. A., Wevers,
I., McCreath, W., Kyrölä, E., Oikarinen, L., Leppelmeier, G. W., Auvinen, H., Mégie, G., Hauchecorne, A., Lefèvre, F., de La Nöe, J.,
585   Ricaud, P., Frisk, U., Sjoberg, F., von Schéele, F., and Nordh, L.: The OSIRIS instrument on the Odin spacecraft, Canadian Journal of
Physics, 82, 411–422, https://doi.org/10.1139/p04-005, https://doi.org/10.1139/p04-005, 2004.
López-Puertas, M., García-Comas, M., Funke, B., Gardini, A., Stiller, G. P., Von Clarmann, T., Glatthor, N., Laeng, A., Kaufmann, M.,
Sofieva, V. F., Froidevaux, L., Walker, K. A., and Shiotani, M.: MIPAS observations of ozone in the middle atmosphere, Atmospheric
Measurement Techniques, 11, 2187–2212, https://doi.org/10.5194/amt-11-2187-2018, 2018.
590   Marsh, D., Smith, A., Brasseur, G., Kaufmann, M., and Grossmann, K.: The existence of a tertiary ozone maximum in the high-latitude
middle mesosphere, Geophysical Research Letters, 28, 4531–4534, https://doi.org/10.1029/2001GL013791, 2001.
McDade, I., Murtagh, D., Greer, R., Dickinson, P., Witt, G., Stegman, J., Llewellyn, E., Thomas, L., and Jenkins, D.: ETON 2: Quenching
parameters for the proposed precursors of O2(b1Σg+) and O(1S) in the terrestrial nightglow, Planetary and Space Science, 34, 789–800,
https://doi.org/10.1016/0032-0633(86)90075-9, 1986.

595   McLinden, C. A., Fioletov, V. E., Haley, C. S., Lloyd, N., Roth, C., Degenstein, D., Bourassa, A., McElroy, C. T., and Llewellyn, E. J.: An evaluation of Odin/OSIRIS limb pointing and stratospheric ozone through comparisons with ozonesondes, Canadian Journal of Physics, 85, 1125+, 2007.

Mlynczak, M. G., Solomon, S., and Zaras, D. S.: An updated model for O2(a1Δg) concentrations in the mesosphere and lower thermosphere and implications for remote sensing of ozone at 1.27 μm, Journal of Geophysical Research: Atmospheres, 98, 18 639–18 648,
600   https://doi.org/10.1029/93JD01478, 1993.

Mlynczak, M. G., Morgan, F., Yee, J. H., Espy, P., Murtagh, D., Marshall, B., and Schmidlin, F.: Simultaneous measurements of the O2(1Δ) and O2(1Σ) airglows and ozone in the daytime mesosphere, Geophysical Research Letters, 28, 999–1002, https://doi.org/10.1029/2000GL012423, 2001.

Mlynczak, M. G., Marshall, B. T., Martin-Torres, F. J., Russell, J. M., Thompson, R. E., Remsberg, E. E., and Gordley, L. L.: Sound-
605   ing of the Atmosphere using Broadband Emission Radiometry observations of daytime mesospheric O2 (1Δ) 1.27 μm emission and derivation of ozone, atomic oxygen, and solar and chemical energy deposition rates, Journal of Geophysical Research Atmospheres, 112, https://doi.org/10.1029/2006JD008355, 2007.

Murtagh, D., Frisk, U., Merino, F., Ridal, M., Jonsson, A., Stegman, J., Witt, G., Eriksson, P., Jiménez, C., Megie, G., De la Noë, J., Ricaud, P., Baron, P., Pardo, J. R., Hauchcorne, A., Llewellyn, E. J., Degenstein, D. A., Gattinger, R. L., Lloyd, N. D., Evans, W. F., McDade,
610   I. C., Haley, C. S., Sioris, C., Von Savigny, C., Solheim, B. H., McConnell, J. C., Strong, K., Richardson, E. H., Leppelmeier, G. W., Kyrölä, E., Auvinen, H., and Oikarinen, L.: An overview of the Odin atmospheric mission, Canadian Journal of Physics, 80, 309–319, https://doi.org/10.1139/P01-157, 2002.

Murtagh, D., Skyman, A., Rydberg, B., and Eriksson, P.: Odin/SMR Diagnostic Dataset: Technical Note, Tech. rep., https://odin.rss.chalmers. se/static/documents/DDS.pdf, 2018.

615   Picone, J. M., Hedin, A. E., Drob, D. P., and Aikin, A. C.: NRLMSISE-00 empirical model of the atmosphere: Statistical comparisons and scientific issues, Journal of Geophysical Research: Space Physics, 107, https://doi.org/10.1029/2002JA009430, 2002.

R. J. Thomas, C. A. Barth, G. J. Rottman, D. W. Rusch, G. H. Mount, G. M. Lawrence, R. W. Sanders, G. E. Thomas, and L. E. Clemens: Ozone density distribution in the mesosphere (50-90 km) measured by the SME limb scanning near infrared spectrometer, Geophysical Research Letters, https://doi.org/10.1029/gl010i004p00245, 1983.

620   Rodgers, C. D.: Inverse methods for atmospheric sounding : theory and practice., Series on atmospheric, oceanic and planetary physics: 2, World Scientific, http://search.ebscohost.com/login.aspx?direct=true&AuthType=sso&db=cat07470a&AN=clc. 8b34e549d2e147e7ad113df41218f018&site=eds-live&scope=site&custid=s3911979&authtype=sso&group=main&profile=eds, 2000.

Sheese, P.: Mesospheric ozone densities retrieved from OSIRIS observations of the O2 A-band dayglow, Ph.D. thesis, 2009.

Smith, A. K., Harvey, V. L., Mlynczak, M. G., Funke, B., García-Comas, M., Hervig, M., Kaufmann, M., Kyrölä, E., Lõpez-Puertas, M.,
625   McDade, I., Randall, C. E., Russell, J. M., Sheese, P. E., Shiotani, M., Skinner, W. R., Suzuki, M., and Walker, K. A.: Satellite observations of ozone in the upper mesosphere, Journal of Geophysical Research Atmospheres, 118, 5803–5821, https://doi.org/10.1002/jgrd.50445, 2013.

Smith, A. K., Espy, P. J., López-Puertas, M., and Tweedy, O. V.: Spatial and Temporal Structure of the Tertiary Ozone Maximum in the Polar Winter Mesosphere, Journal of Geophysical Research: Atmospheres, 123, 4373–4389, https://doi.org/10.1029/2017JD028030, 2018.

630   Sofieva, V. F., Rahpoe, N., Tamminen, J., Kyrölä, E., Kalakoski, N., Weber, M., Rozanov, A., Von Savigny, C., Laeng, A., Von Clarmann, T., Stiller, G., Lossow, S., Degenstein, D., Bourassa, A., Adams, C., Roth, C., Lloyd, N., Bernath, P., Hargreaves, R. J., Urban, J., Murtagh,

Atmospheric
Measurement
Techniques
Discussions

D., Hauchecorne, A., Dalaudier, F., Van Roozendael, M., Kalb, N., and Zehner, C.: Harmonized dataset of ozone profiles from satellite limb and occultation measurements, Earth System Science Data, 5, 349–363, https://doi.org/10.5194/essd-5-349-2013, 2013.

Sofieva, V. F., Kalakoski, N., Päivärinta, S. M., Tamminen, J., Laine, M., and Froidevaux, L.: On sampling uncertainty of satellite ozone
635   profile measurements, Atmospheric Measurement Techniques, 7, 1891–1900, https://doi.org/10.5194/amt-7-1891-2014, 2014.

Thomas, R. J., Barth, C. A., Rusch, D. W., and Sanders, R. W.: Solar Mesosphere Explorer near-infrared spectrometer: measurements of 1.27 micrometer radiances and the inference of mesospheric ozone., Journal of Geophysical Research, https://doi.org/10.1029/JD089iD06p09569, 1984.

Van Der A, R., Adams, C., Bernath, P., Von Clarmann, T., Coldewey-Egbers, M., Degenstein, D., Dudhia, A., Hargreaves, R., Laeng, A.,
640   Lerot, C., Loyola, D., Van Peet, J., Rahpoe, N., Sofieva, V., Stiller, G., Tamminen, J., Urban, J., Roozendael, M. V., Weber, M., Lerot, C., Danckaert, T., Astoreca, R., Heue, K.-P., Sheese, P., Walker, K., and Tukiainen, S.: Ozone CCI Algorithm Theoretical Basis Document Phase 2 Version 2 (ATBDv2), Tech. rep., http://cci.esa.int/sites/default/files/filedepot/incoming/Ozone_cci_ATBD_Phase2_V2.pdf, 2017.

Yankovsky, V. A. and Manuilova, R. O.: Model of daytime emissions of electronically-vibrationally excited products of O_3 and O_2 photolysis: application to ozone retrieval, Annales Geophysicae, 24, 2823–2839, https://doi.org/10.5194/angeo-24-2823-2006, https://
645   www.ann-geophys.net/24/2823/2006/, 2006.

Yankovsky, V. A., Martyshenko, K. V., Manuilova, R. O., and Feofilov, A. G.: Oxygen dayglow emissions as proxies for atomic oxygen and ozone in the mesosphere and lower thermosphere, Journal of Molecular Spectroscopy, 327, 209–231, https://doi.org/10.1016/j.jms.2016.03.006, 2016.

Zarboo, A., Bender, S., Burrows, J. P., Orphal, J., and Sinnhuber, M.: Retrieval of $O2(1\Sigma)$ and $O2(1\Delta)$ volume emission rates in
650   the mesosphere and lower thermosphere using SCIAMACHY MLT limb scans, Atmospheric Measurement Techniques, 11, 473–487, https://doi.org/10.5194/amt-11-473-2018, 2018.

Zhu, X., Yee, J. H., and Talaat, E. R.: Effect of dynamical-photochemical coupling on oxygen airglow emission and implications for daytime ozone retrieved from 1.27 μm emission, Journal of Geophysical Research Atmospheres, 112, https://doi.org/10.1029/2007JD008447, 2007.